applied sciences

MDPI

Article

Semi-Solid Forging Process of Aluminum Alloy Connecting Rods for the Hydrogen Internal Combustion Engine

Yongfei Wang [1,2,3], Hong Jiang [1], Mengjiao Zhang [1], Chaoqun Zhang [1], Shengdun Zhao [1,2,3], Ding Ding [4] and Yi Guo [5,*]

1 School of Mechanical Engineering, Xi'an Jiaotong University, Xi'an 710049, China; wangyongfei324@mail.xjtu.edu.cn (Y.W.)
2 National Key Laboratory of Metal Forming Technology and Heavy Equipment, Xi'an 710049, China
3 Xi'an Key Laboratory of Intelligent Equipment and Control, Xi'an 710049, China
4 Wuhan Second Ship Design and Research Institute, Wuhan 430035, China
5 School of Energy and Power Engineering, Xi'an Jiaotong University, Xi'an 710049, China
* Correspondence: yiguo666@mail.xjtu.edu.cn; Tel.: +86-13201848800

Abstract: As an important piece of equipment for hydrogen energy application, the hydrogen internal combustion engine is helpful for the realization of zero carbon emissions, where the aluminum connecting rod is one of the key core components. A semi-solid forging forming process for the 7075 aluminum alloy connecting rod is proposed in this work. The influence of process parameters, such as the forging ratio, sustaining temperature, and duration time, on the microstructures of the semi-solid blank is experimentally investigated. The macroscopic morphology, metallographic structure, and physical properties of the connecting-rod parts are analyzed. Reasonable process parameters for preparing the semi-solid blank are obtained from the experimental results. Under the reasonable parameters, the average grain size is 41.48~42.57 μm, and the average shape factor is 0.80~0.81. The yield strength and tensile strength improvement ratio of the connecting rod produced by the proposed process are 47.07% and 20.89%, respectively.

Keywords: hydrogen energy; hydrogen internal combustion engine; aluminum alloy connecting rod; semi-solid forging forming; microstructure; mechanical property

check for updates

Citation: Wang, Y.; Jiang, H.; Zhang, M.; Zhang, C.; Zhao, S.; Ding, D.; Guo, Y. Semi-Solid Forging Process of Aluminum Alloy Connecting Rods for the Hydrogen Internal Combustion Engine. *Appl. Sci.* **2024**, *14*, 5219. https://doi.org/10.3390/app14125219

Academic Editor: Maria Amélia Ramos Loja

Received: 27 April 2024
Revised: 12 June 2024
Accepted: 14 June 2024
Published: 16 June 2024

Copyright: © 2024 by the authors. Licensee MDPI, Basel, Switzerland. This article is an open access article distributed under the terms and conditions of the Creative Commons Attribution (CC BY) license (https://creativecommons.org/licenses/by/4.0/).

1. Introduction

Hydrogen has the characteristics of an extremely high energy density, wide production method, and environmental friendliness, and it is suggested that it will replace fossil energy [1]. Hydrogen can also be used as a long-term energy storage medium to offset the disadvantages of randomness and volatility of solar energy, wind energy, and other green energy sources [2,3]. Therefore, hydrogen fuel is regarded as an important energy carrier in the future. In the vehicle-power field, fuel cells are the main application scenario for hydrogen fuel, gaining a lot of technological progress in the last decades [4].

In recent years, the hydrogen internal combustion engine (HICE) has received renewed attention as one of the optional technologies for achieving a zero-carbon emission society [5,6]. The HICE can capitalize on the existing industrial base for internal combustion engines. Its application in automotive power helps to increase the hydrogen demand, thus contributing to the hydrogen infrastructure's development [7].

As shown in Figure 1, the HICE mainly includes a crankshaft, connecting rod, piston, combustion chamber, intake port, and exhaust port [8–10]. During the operation of a HICE, the connecting rod is subjected to complex loads, including bending and alternating tension and pressure; thus, it is an important component of a HICE [11–13]. The material, producing process, and manufacturing quality of connecting rods are significant to the performance of the whole HICE. An example of the connecting rod with a specific shape and dimensions for the HICE is shown in Figure 1.

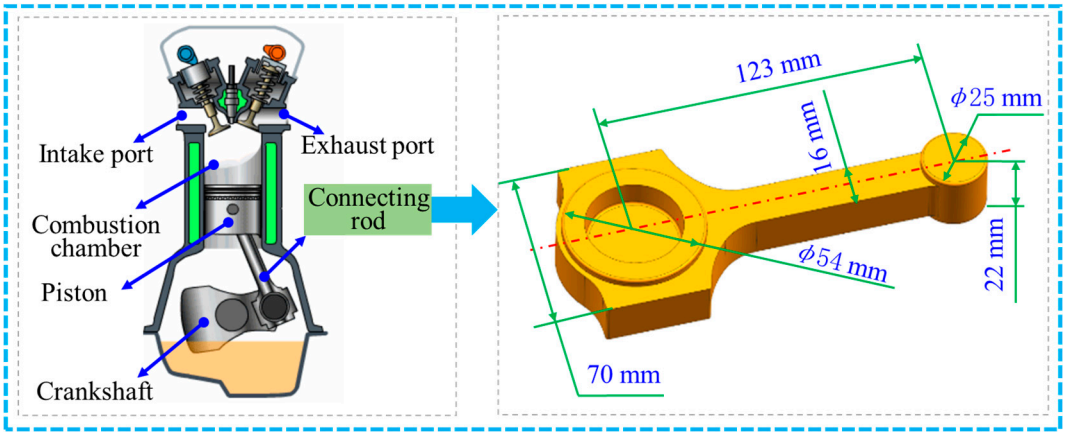

Figure 1. Shape and dimension of connecting rod for the HICE.

As one of the important force transmission parts for the internal combustion engine, the connecting rod is often machined and manufactured with steel, cast iron, iron-based powder, and other materials [14–17]. With the increasing demand for lightweight automotive components in the market, high-strength aluminum alloy materials have attracted extensive attention from many scholars and businessmen in the connecting-rod-manufacturing field [18–20]. As a representative of high-strength aluminum alloy, the 7075 aluminum alloy has numerous merits, such as low density, lightweight, and high strength. It is, therefore, gradually applied to manufacturing various automobile parts and is regarded as a promising manufacturing material for the connecting rod of a HICE. The mechanical properties of connecting rods for HICEs not only depend on the material itself but are also affected by the manufacturing process.

Traditional manufacturing processes for connecting rods include hot forging [21–23], powder metallurgy [24], liquid-die forging [25], and die casting [26]. Although the above methods can obtain connecting rods with high dimensional accuracy and qualified mechanical properties, these methods have some shortcomings as follows. The forging force for the hot-forging process is large, requiring special large equipment and high equipment costs [27]. The die-casting process is prone to shrinkage porosity, shrinkage cavity, insufficient filling, and other defects within the connecting rod. The costs of molds and samples for the powder metallurgy process in small-batch production are high. In terms of liquid-die forging, it is risky to premature solidification at thin-walled and fine structures, which affects the quality of the connecting rods. It is a challenge for the liquid-die forging to produce the connecting rode with a reduced scrap rate. Therefore, there is an urgent need to explore a new connecting-rod forming process for providing an improved solution for the manufacturing of 7075 aluminum alloy connecting rod applications in the HICE.

Semi-solid forming of metal (SSFM) is an innovative metal-forming technique initially introduced by Professor Flemings and his team at MIT [28]. This method has since been extensively applied and explored by various researchers [29–31]. In the SSFM process, semi-solid materials with fine and spherical grains are first produced. Subsequently, components with refined microstructures and superior performance can be fabricated through techniques such as extrusion, forging, rolling, or die casting [32,33]. The SSFM process can also operate through stages, including the first cooling or solidifying the semi-solid blank into a solid blank and then reheating and forming the solid blank with suitable dimensions according to the production demands [34–36]. The SSFM process combines the advantages of liquid casting forming and solid plastic forming, as it has excellent flow mobility in the material and high physical properties in the product, which is regarded as one of the most potential green forming technologies [37–39].

The SSFM process mainly contains procedures, which are the preparation of the semi-solid blank and the formation of a part, which has received extensive attention in recent years [40–43]. Jiang et al. [44] investigated the influences of treatment temperature and

maintaining time on the microstructures of hot extruded 7075 aluminum alloy during the isothermal heat treatment (IHT). They found that the microstructures, with an average grain dimension (AGD) of about 65~85 μm and average shape factor (ASF) of about 0.74~0.79, can be obtained by the optimum process parameters, with the isothermal temperature of 600~610 °C and the holding time of 10~15 min. Furthermore, Jiang et al. [45] used the semi-solid material combing the extrusion forming process to successfully produce the 7075 aluminum alloy deep-cavity cylinder with a tensile strength of 315.26 MPa. Fu et al. [46] prepared semi-solid 7075 aluminum alloy blanks through a modified strain-induced melt activation (SIMA) process, which includes equal-channel angular pressing (ECAP) deformation and IHT. They reported that the AGD of the prepared blank enlarged when the process temperature was elevated or with a decrease in the deformation pass. Moreover, the tensile strength of the semi-solid samples was improved by increasing the deformation pass of ECAP. Binesh et al. [47] applied repetitive upsetting extrusion (RUE) in the recrystallization and partial remelting (RAP) process to obtain a semi-solid 7075 aluminum alloy blank. They found that the AGD can be reduced by increasing the RUE cycles and, therefore, improve the grain spheroidization degree. The thixoextrusion process was adopted by Liu et al. [48] to form a complex 7075 aluminum alloy elbow part. In their work, the effect of the second phase on the performance of the part was analyzed. Meshkabadi et al. [49] demonstrated that the parallel tubular channel angular pressing process can produce a semi-solid 7075 aluminum tube with an excellent metallographic structure.

Though the SSFM process has received extensive attention from many researchers, the 7075 aluminum alloy connecting rod for the HICE formed by the semi-solid forging forming (SSFF) process has not been reported. A novel SSFF process, including radial forging plastic deformation (RFPD), isothermal heating treatment (IHT), and forging forming, is proposed to produce the 7075 aluminum alloy connecting rod (AACR) for the HICE in this work in order to solve the shortages of the existing connecting-rod manufacturing process. The effect of process parameters, such as forging ratio (FR), sustaining temperature (ST), and duration time (DT), on the microstructures of 7075 aluminum alloy is investigated. The macroscopic morphology, metallographic structure, and physical properties of the AACR formed by the SSFF and solid forging forming (SFF) processes were compared and analyzed. This work can provide a feasible new process for manufacturing 7075 AACRs for HICE.

2. Materials and Methods

2.1. Semi-Solid Forging Forming Scheme for the Aluminum Alloy Connecting Rod

In this paper, the annealed 7075 wrought aluminum extruded blank is used as the raw material, and it has a diameter of 90 mm and a length of 800 mm. The material constituents and their content ratios are summarized in Table 1 and were determined by the Xi'an Litong Electromechanical Equipment Manufacturing Co., LTD. The semi-solid range of this material was determined by using the "NETZSCH STA 449F5 (NETZSCH Corporation, Bavarian Asia, Germany)" equipment for the differential scanning calorimeter (DSC) experiment, in which the samples were heated to 700 °C at a rate of 10 °C/min under a nitrogen atmosphere. The solidus and liquidus temperatures of the material are 591 °C and 656 °C, respectively, which are obtained by the DSC curve, as shown in Figure 2a. Through integrating the DSC curve, the variation in the solid fraction with temperature can be obtained as presented in Figure 2b. As shown in Figure 2b, when the temperature is higher than 630 °C, the solid fraction of 7075 aluminum alloy decreases fast, indicating that the liquid fraction increases rapidly. This might cause liquid segregation in the SSFF process, resulting in a reduction in the quality of the formed parts. It was reported that semi-solid materials with a solid fraction higher than 60% are suggested for the SSFF process, where the AGD is less than 100 um and the ASF is more than 0.6 [50,51]. Therefore, the temperature is set to less than or equal to 630 °C in the semi-solid isothermal treatment (SSIT) process in this study.

Table 1. Chemical composition of the 7075 aluminum alloy.

Element	Si	Fe	Cu	Mn	Mg	Cr	Zn	Ti	Al
wt.%	0.08	0.19	1.47	0.02	2.25	0.21	5.22	0.04	Bal.

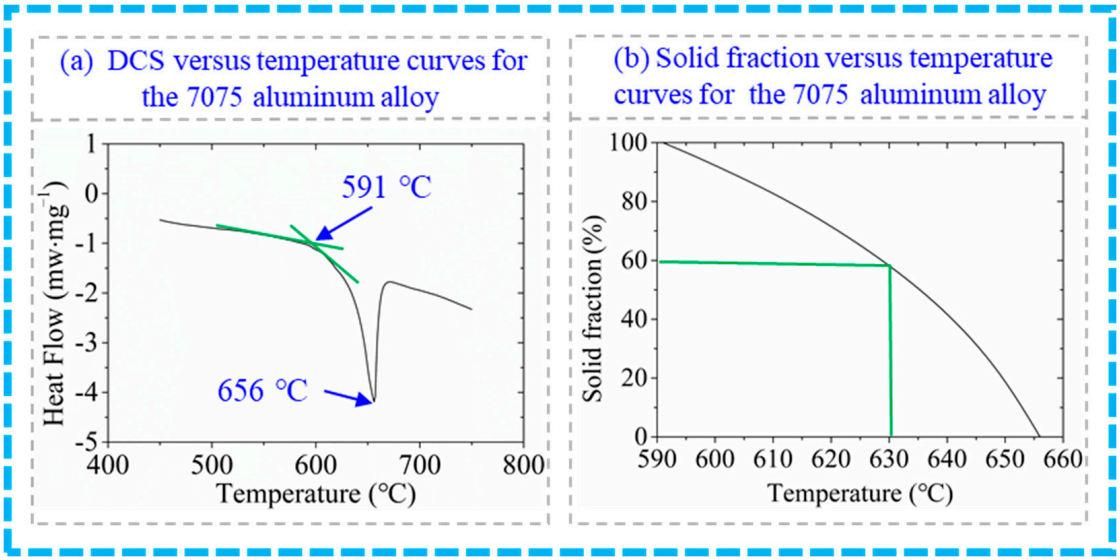

Figure 2. DSC and solid fraction curve of 7075 aluminum alloy.

The SSFF process of the connecting rod can be divided into three stages, as shown in Figure 3. The first stage is the RFPD of the aluminum alloy bar. The working principle of the RFPD is presented in Figure 3a. The rotary metal blank is fed along the axial direction. At the same time, a high-frequency reciprocating forging for the metal blank is carried out by four hammer dies distributed along the radial direction of the metal blank. In this stage, the relative forging ratio (FR) can be adjusted by changing the diameter of the RF-deformed stepped bar. The second stage is the IHT process. The RF-deformed blanks with different FRs are located in the resistance heating furnace for IHT to prepare a semi-solid blank (SSB). In this stage, the quality of SSB is influenced by three process parameters, including FR, ST, and DT. The third stage is the forging-forming process of the connecting rods. The SSB with the ideal microstructure prepared in the second stage is placed into the die cavity shown in Figure 3c, and then, the connecting rod's parts can be formed when the forging process is finished.

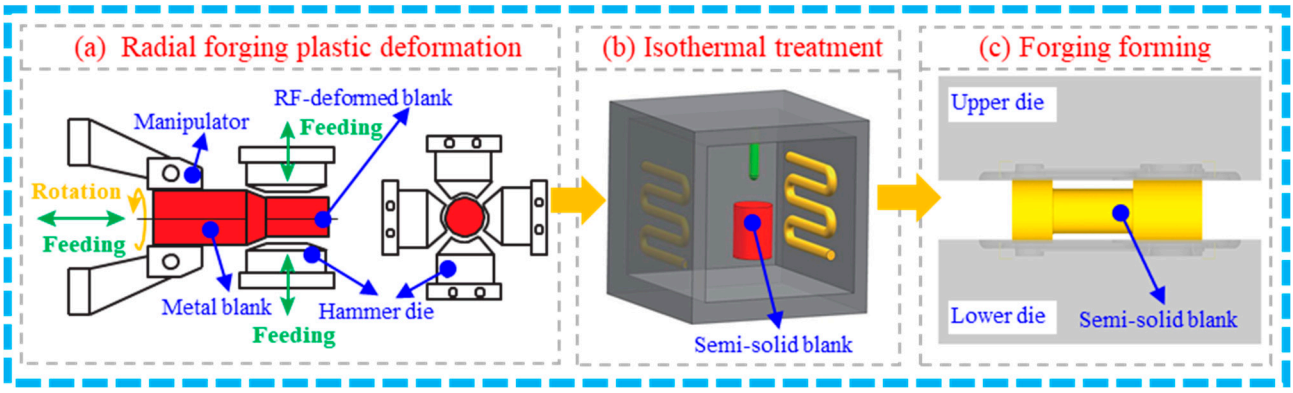

Figure 3. SSFF scheme for the aluminum alloy connecting rod.

2.2. Experimental Procedure of the SSFF Process for the Connecting Rod

The experimental press machine and SSFF die for the connecting rod are shown in Figure 4. Table 2 shows the process parameters used in the test process. First, to obtain the reasonable process parameters for the ideal SSB, as shown in Group I, the RF-deformed blanks with different FRs are treated at 630 °C with a time of 9 min to analyze the effects of FR on the microstructures. In this group, the 7075 aluminum alloy with a diameter of 90 mm is radially forged to obtain an RF-deformed stepped bar with diameters of 75 mm, 68 mm, 62 mm, and 45 mm for the FR of 30.56%, 42.91%, 52.54%, and 75%, respectively. The qualities of the semi-solid blanks with different FRs are analyzed to identify the reasonable FR. Then the RF-deformed blanks with the reasonable FRs are heated at the ST of 610 °C, 620 °C, and 630 °C. At each ST, the blank is treated for three different DTs of 3 min, 6 min, and 9 min. Therefore, the influence of ST and DT on the microstructures can be obtained through experiments in Groups II, III, and IV. Based on the results from experiments in Groups I, II, III, and IV, the optimal parameters for SSB can be identified. Then, in Group V, the AACR is produced by the forging forming of the ideal SSB. In Group VI, the RF-deformed blank under the reasonable FR is heated with the ST of 590 °C and DT of 10 min, which provides the material for the AACR production by forging forming. In both Groups V and VI, the die temperature is 250 °C, while the forging speed is 10 mm/s. Groups V and VI are designed to form the AACR by both SSFF and SFF tests for the comparison of their quality, which aims to verify the advancement of the SSFF process for manufacturing the connecting rod.

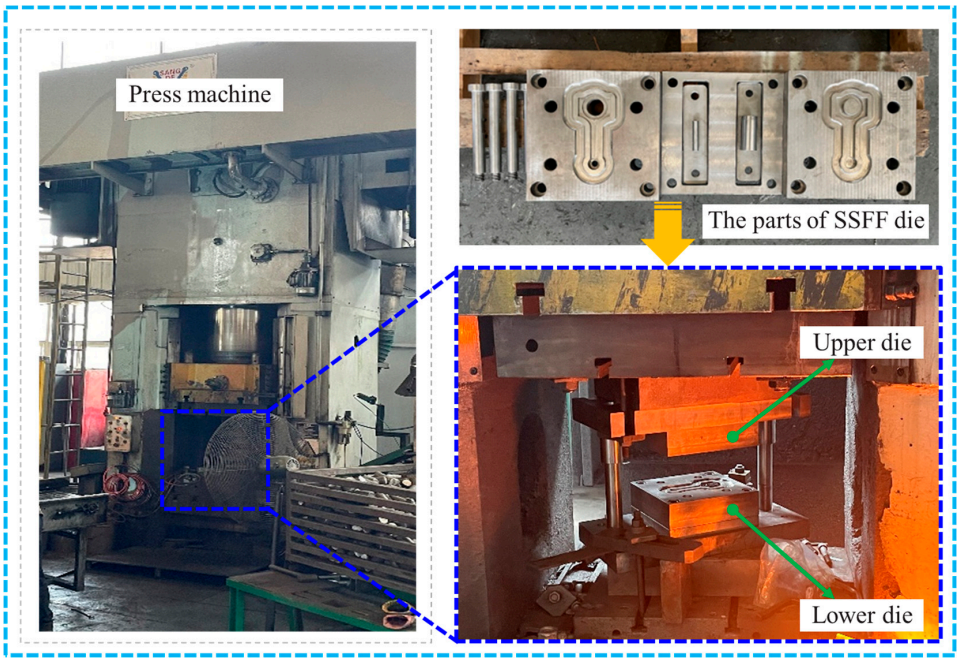

Figure 4. The experimental press machine and SSFF die for the connecting rod.

Table 2. Process parameters for the SSFF of connecting rod in this work.

Group No.	Items	Forging Ratio	Sustaining Temperature (°C)	Duration Time (min)
I	IHT process	30.56%, 42.91%, 52.54% and 75%	630	9
II		Reasonable FR	610	3, 6, 9
III		Reasonable FR	620	3, 6, 9
IV		Reasonable FR	630	3, 6, 9

Table 2. *Cont.*

Group No.	Items	Forging Ratio	Sustaining Temperature (°C)	Duration Time (min)
	SSFF and SFF process	Forming material	Die temperature (°C)	Forging Speed (mm/s)
V		Semi-solid billet prepared by IHT process with reasonable process parameters	250	10
VI		Billet prepared by isothermal treatment with the 590 °C and 10 min	250	10

The quality of the semi-solid billet and the AACR is presented by the microstructure and tensile property analysis. To investigate the effect of process parameters, such as forging ratio, sustaining temperature, and duration time, on the microstructures of the semi-solid blank, the samples are cut from the RF-deformed blank with different FRs. To study the microstructure and tensile property of the AACR, samples are obtained from the positions as shown in Figure 5 for the microstructure and tensile analysis. The sample dimensions for the strength testing are shown in Figure 5b. A universal material testing machine (Instron-5982) is used for the strength testing, and the tensile rate of this machine is 1.25 mm/min. The microstructure samples are ground, polished, and etched for 90 s in the hydrofluoric acid solution. The optical microscope (NIKON ECLIPSE LV 150N) is adopted in the study to analyze the metallographic structure. The AGD and ASF of the metallographic structure can be calculated by Equations (1) and (2), respectively. The tensile property of the forming connecting rod is obtained by a material testing machine.

$$\mathrm{AGD} = \frac{\sum_{N=1}^{N} \sqrt{4A/\pi}}{N} \tag{1}$$

$$\mathrm{ASF} = \frac{\sum_{N=1}^{N} 4\pi A/P^2}{N} \tag{2}$$

where A is the effective area of one solid grain, P is the perimeter of one solid grain, and N is the grain number.

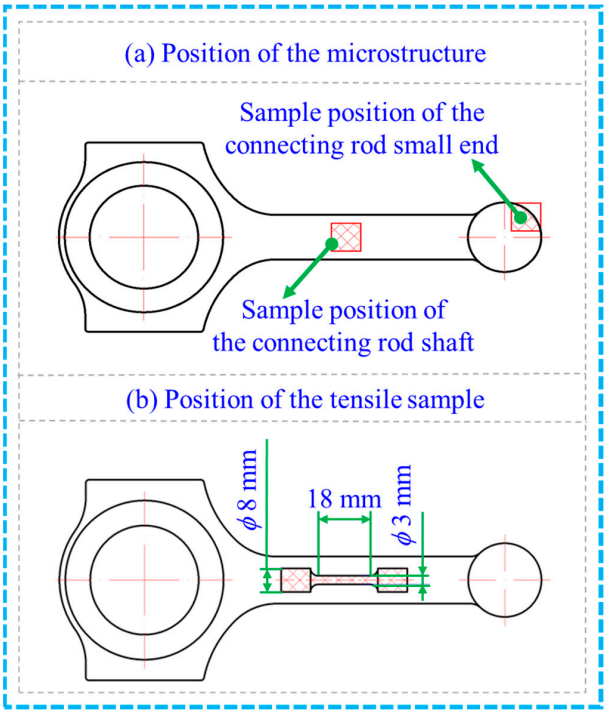

Figure 5. Microstructure and tensile sample position of the forming connecting rod.

3. Results and Discussion

3.1. Effect of FR on the 7075 Aluminum Alloy Blank

Figure 6 shows the macro-morphology of an aluminum alloy blank deformed by the RF process under varied values of FRs. As shown in Figure 6a, the RF-deformed 7075 aluminum alloy blank had four different diameters, indicating the FRs of 30.56%, 42.91%, 52.54%, and 75%, respectively. The value of the FR increases with the decrease in the diameter, which represents an elevation in the strain energy stored in the RF-deformed blank, when the diameter decreases under the RFPD process [52]. As presented in Figure 6b–e, the RF-deformed blanks with different FRs had smooth surfaces without any defects, such as surface cracks or pits, which indicated that the 7075 aluminum alloy with a diameter of 90 mm used in this work can be successfully deformed by the RFPD process, with an FR up to 75%. Moreover, some characteristic lines (marked with a red A) can be obviously seen in Figure 6b–e, which can be attributed to the deformed process of RFPD in this work. During the RFPD process [53–55], the rotary 7075 aluminum blank is fed along the axial direction. Meanwhile, a high-frequency reciprocating forging for the 7075 aluminum blank is carried out by four hammer dies distributed along the radial direction of this blank. Therefore, the characteristic lines appeared on the outer surface of the RF-deformed 7075 aluminum alloy blank.

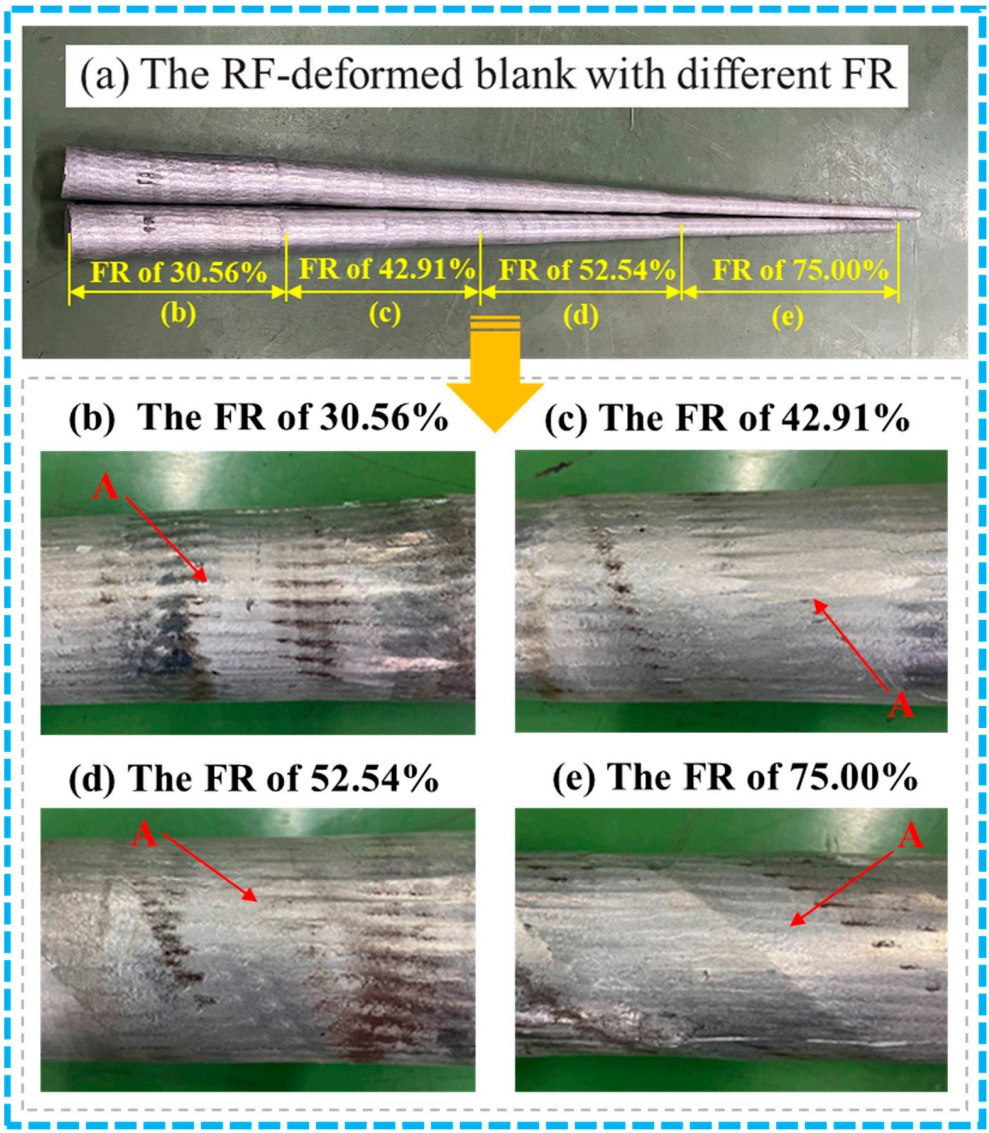

Figure 6. Effect of FR on the macro-morphology of the aluminum alloy blank.

Figure 7 shows the effect of FR on the metallographic structure of the aluminum alloy blank. The longitudinal and transverse sections of the metallographic structure for the 7075 aluminum alloy are shown in Figure 7a,b, respectively. The directionality was more obvious in the longitudinal microstructure of the 7075 aluminum alloy bar along the extrusion direction, while the microstructure of the transverse section was more uniform. The above phenomenon was mainly determined by the initial state of the microstructure for the 7075 aluminum alloy blank. The 7075 aluminum alloy blank used in this work was in the extruded state, which was formed by the hot-extrusion process. Therefore, the longitudinal section microstructure of this blank might be distributed along the extrusion direction. It was also shown that, despite the subsequent annealing treatment being performed for this extruded blank, it was not possible to completely eliminate the deformed fibrous microstructures obtained by the extrusion process.

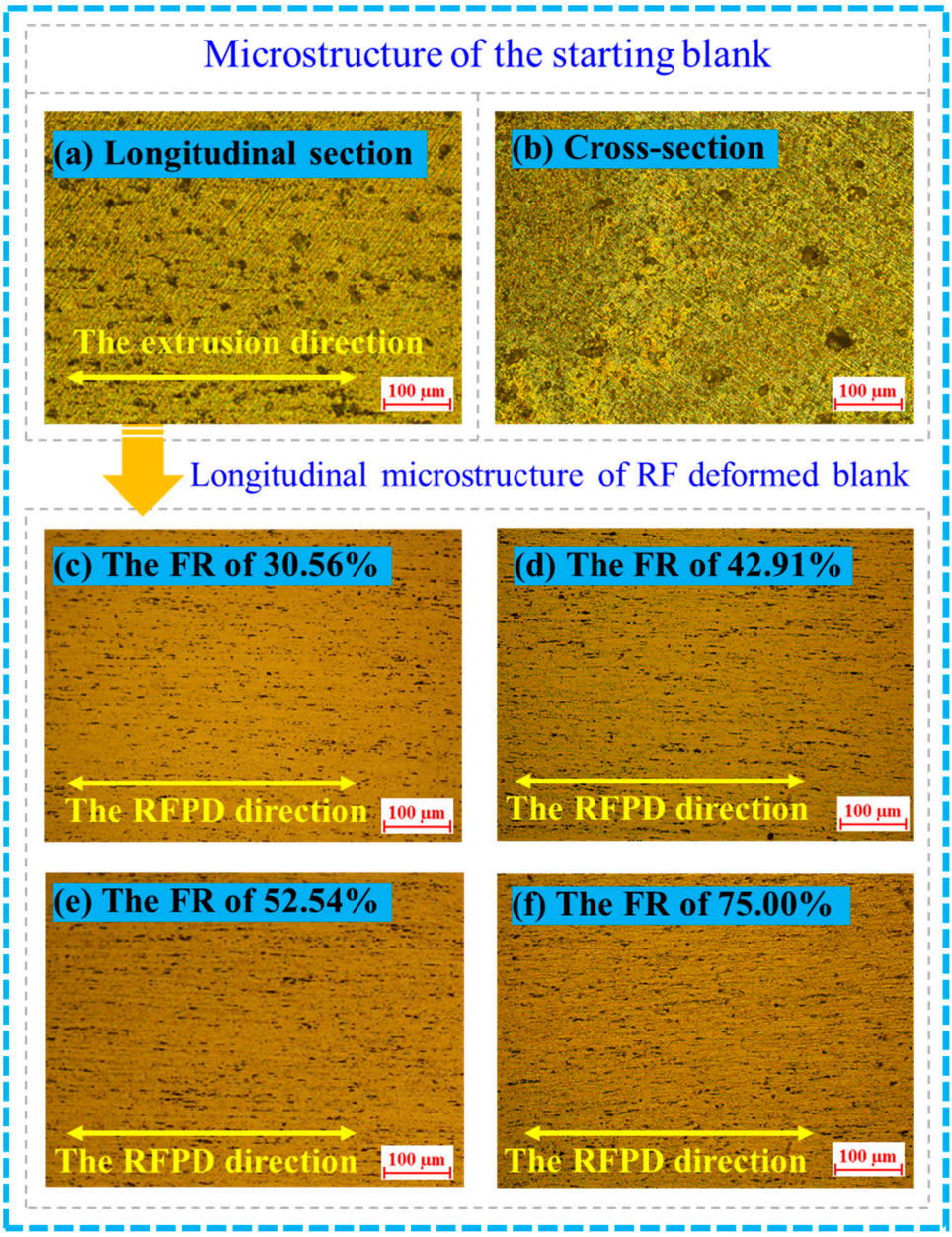

Figure 7. Effect of FR on the microstructure of the aluminum alloy blank.

According to the principle of the RFPD process [54,56], the main deformation mode in the RFPD process is radial reduction rather than torsion deformation. Therefore, the

longitudinal section microstructure of the RF-deformed blank is more important for us to investigate the effect of FR on the microstructures of the RF-deformed 7075 aluminum alloy blank in this work. The microstructures shown in Figure 7c–f are the experimental results corresponding to the longitudinal section microstructure of the RF-deformed blank with different FRs shown in Figure 6b–e, respectively. Comparing Figure 7a,c, it can be seen that, after applying RFPD with an FR of 30.56% to 7075 aluminum alloy blank, its microstructure changed significantly, where the fibrous microstructure distributed along the RFPD direction. The densification degree of the fibrous microstructure in Figure 7c increased significantly compared to Figure 7a. As shown in Figure 7d, the densification degree of the fibrous microstructure further increased when the FR was 42.91%, but the difference in densification degree for the fibrous microstructure was not obvious as the FR further increased to 52.54% or 75%. It showed that, after the RFPD process of 7075 aluminum alloy blank, the densification degree of its fibrous microstructure gradually increased with increasing the FR, but the deformation degree tended to be stable when its FR exceeded 52.54%.

3.2. Effect of the Isothermal Process on the RF-Deformed Blank

The longitudinal section microstructures of the RF-deformed blank after SSIHT at 620 °C for 9 min are shown in Figure 8, in which the FRs of the RF-deformed blank are 30.56%, 42.91%, 52.54%, and 75.00%. Comparing Figures 7 and 8, it reveals that, after the RF-deformed blank with different FRs was treated at the temperature of 620 °C for 9 min, its microstructure transformed from a fibrous deformation microstructure to a semi-solid microstructure, where a uniform distribution of a large number of solid grains was observed in the liquid phase. This was mainly because a large amount of strain energy was accumulated in the aluminum alloy blank after the RFPD process. However, in the subsequent IHT process, this accumulated strain energy was released, which promoted grain recrystallization and growth. At the same time, the above phenomena also indicated that the RFSIMA process including RFPD, and the followed IHT can be successfully used to produce 7075 aluminum alloy SSB with fine and spherical microstructures.

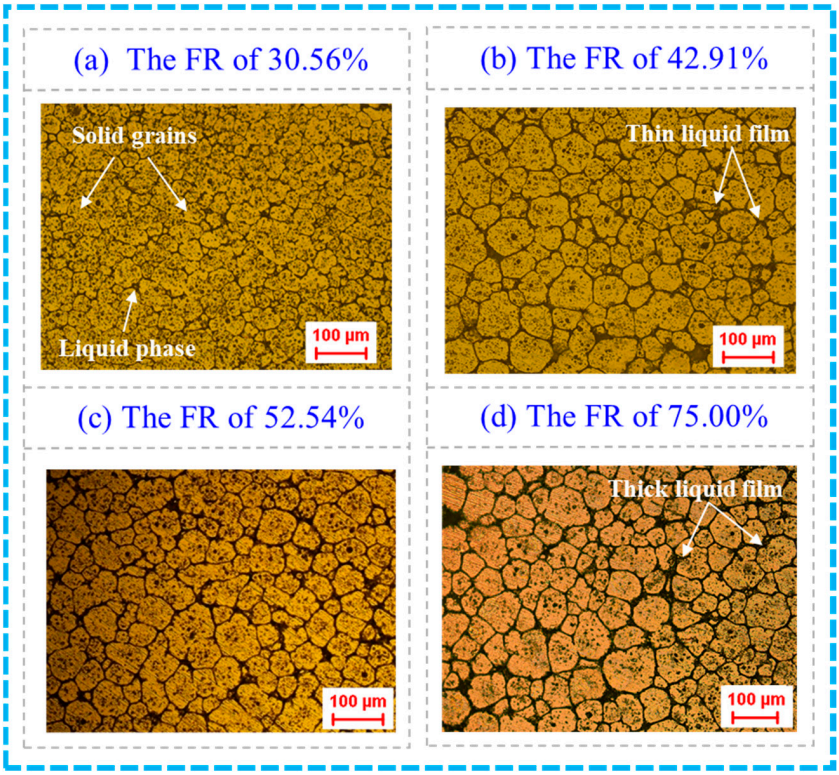

Figure 8. Microstructure of the RF-deformed blank after SSIHT at 620 °C for 9 min.

As shown in Figure 8a, when the FR was 30.56%, more solid grains can be observed, but most of them were bonded together. This was because, at a low FR, relatively low energy was accumulated in the material, which resulted in less liquid phase generated during the IHT process. As the FR increased to 42.91%, the AGS in the microstructure was 42.64 μm with an ASF of 0.78. Thin liquid films can be seen in the microstructure, as shown in Figure 8b, which effectively separated the solid grains. As presented in Figure 8c,d, the thickness of the liquid film increased, and the distribution of the solid grain was more uniform when the FR increased to 52.54% or 75%. Their AGSs were found to be 41.92 and 42.57 μm, with ASFs of 0.80 and 0.81, respectively. According to the analysis results, it can be seen that, when the FR increased from 42.91% to 75%, the thickness of the liquid film in the microstructure enlarged, where no significant change in the grain size was observed. However, the spheroidizing feature in the microstructure was improved when the FR increased to 75%. This increase in the thickness of the liquid film and the grain spheroidizing effect would contribute to the flowability improvement of the SSB during the SSFM process. Hence, the FR of 75% was a reasonable process parameter for preparing the 7075 aluminum alloy SSB in this work.

The microstructures of the RF-deformed blank with 75% FR after SSIHT at 610 °C to 630 °C with different duration times are shown in Figure 9. As shown in Figure 9a, the microstructure after IHT with the ST of 610 °C and the DT of 3 min changed slightly compared with the microstructure with 75% FR shown in Figure 7f. The directionality in the whole microstructure along the RFPD direction was obvious, which was mainly attributed to the fact that the DT was too short for the generation of blank recrystallization. When the duration time was extended to 6 min, a small number of recrystallized grains appeared, which can be seen in Figure 9b. As presented in Figure 9c, when the DT was further extended to 9 min, a large number of fine solid grains appeared in the microstructure, but these grains were bonded together due to the low liquid fraction caused by the low ST. As depicted in Figure 9d–f, when the ST increased to 620 °C, a large number of fine recrystallized grains bonded together can be seen when the DT is 3 min. When the DT extended to 6 min at an ST of 620 °C, more obvious fine solid grains, as well as liquid films, can be seen. When the DT further increased to 9 min, the thickness of the liquid film enlarged, which can effectively separate the solid grains, where fine, uniformly distributed semi-solid spherical grains were obtained.

As shown in Figure 9g, when the ST increased to 630 °C, relatively small semi-solid spherical grains can be seen when the DT is 3 min. At this condition, the liquid film thickness and the grain dimension were basically the same as the microstructures in Figure 9e, where the ST was 620 °C and the DT was 6 min. However, some of the grains were still bonded together due to the low liquid fraction resulting from the short duration of time. When the duration time was extended to 6 min, the liquid fraction increased, and the liquid film uniformly distributed around the solid grains, as illustrated in Figure 9h. Moreover, the AGS was 41.48 μm, and the ASF was 0.8, which was suitable for the SSFF process. However, when the DT extended to 9 min, a large number of as-cast dendritic crystals appeared near the solid grains, which is shown in Figure 9i. This generation of dendritic crystals was because of a rapid quench of the liquid phase that resulted from the melting of some solid grains with the prolonging of the DT at higher temperatures. In addition, the grain size became larger, and its spheroidization degree deteriorated. Although a large number of the liquid phases was produced under the action of high ST and long DT, the liquid-phase distribution was not uniform, resulting in the large solid grains gradually formed by the coarse solid grains that contacted each other [35,57]. Namely, the merging and growth phenomenon of solid grains took place in this condition.

Based on the analysis of the metallographic structure shown in Figures 8 and 9, the influence of process parameters, such as forging ratio, sustaining temperature, and duration time, on the microstructures of the semi-solid blank from Figures 8b–d and 9c,e–i can be summarized in Table 3. Because the microstructures shown in Figures 8a and 9a,b,d are not clear, thus, the AGSs and SFs of solid grains shown in Figures 8a and 9a,b,d are not

calculated in this work. It can be concluded that the semi-solid microstructures shown in Figures 8d and 9f,h are more qualified. Therefore, the reasonable values of the operating parameters for preparing a 7075 aluminum alloy SSB are FR of 75%, ST of 620 °C, and DT of 9 min, or FR of 75%, ST of 630 °C, and DT of 6 min. Under these reasonable operating parameters, the 7075 aluminum alloy SSB can be prepared with an AGS of 41.48~42.57 μm and an ASF of 0.80~0.81.

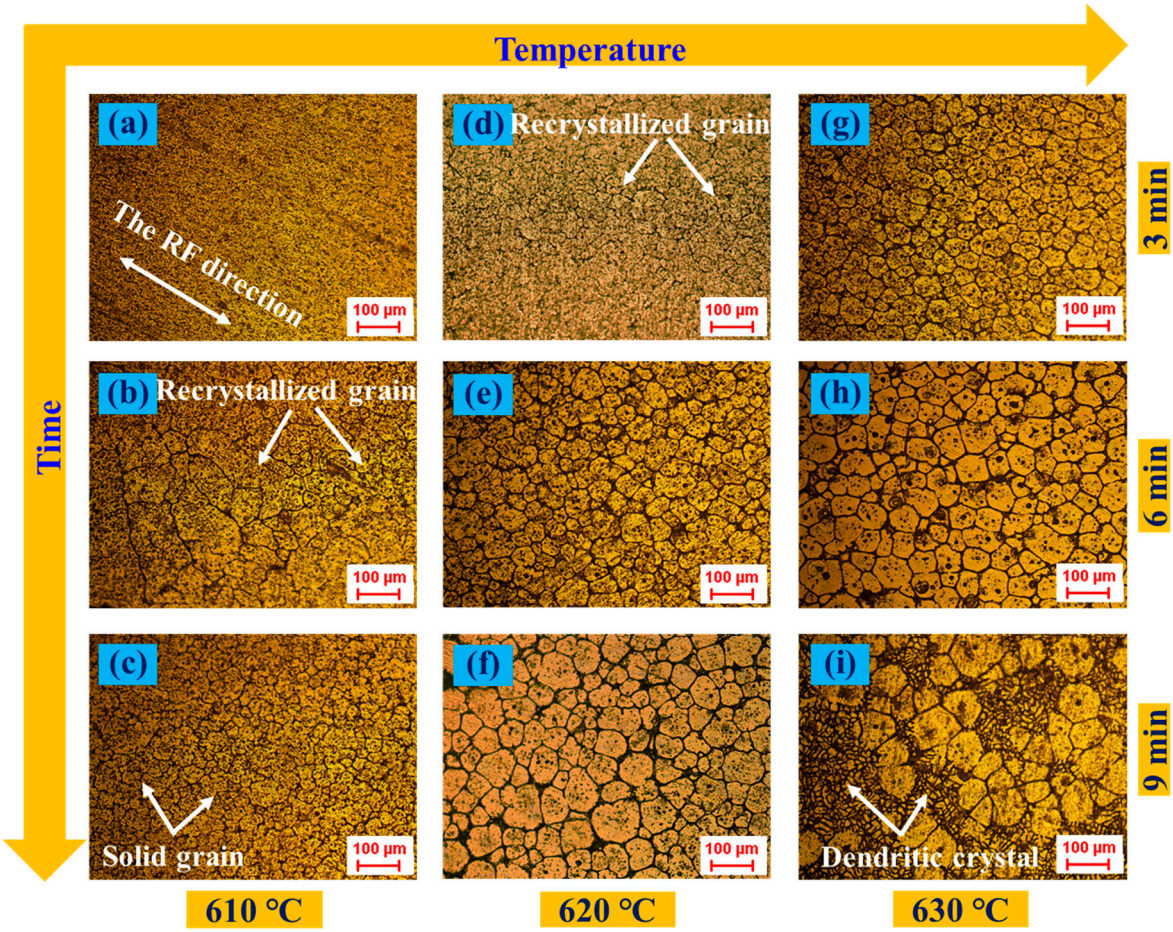

Figure 9. Microstructure of the RF-deformed blank with 75% FR after SSIHT: (**a**) 610 °C, 3 min, (**b**) 610 °C, 6 min, (**c**) 610 °C, 9 min, (**d**) 620 °C, 3 min, (**e**) 620 °C, 6 min, (**f**) 620 °C, 9 min, (**g**) 630 °C, 3 min, (**h**) 630 °C, 6 min, (**i**) 630 °C, 9 min.

Table 3. Influence of process parameters on the AGS and ASF of the SSB.

Forging Ratio	Sustaining Temperature (°C)	Duration Time (min)	Figure	AGS (μm)	ASF
42.91%	620	9	Figure 8b	42.46	0.78
52.54%	620	9	Figure 8c	41.92	0.80
75%	620	9	Figure 8d/Figure 9f	42.57	0.81
75%	610	9	Figure 9c	15.26	0.62
75%	620	6	Figure 9e	26.56	0.67
75%	630	3	Figure 9g	25.54	0.72
75%	630	6	Figure 9h	41.48	0.8
75%	630	9	Figure 9i	56.12	0.76

3.3. Experimental Investigation on the Forming Process of Connecting Rod

The macro-morphology of the connecting rod produced by SSFF and SFF processes is shown in Figure 10, in which three connecting rods are produced by SSFF and SFF processes

with the reasonable operating parameters, respectively. When the process parameters were set as the FR of 75%, ST of 590 °C, and DT of 6 min in the SFF process, the rod shaft and the small end of the connecting rod can be fully formed, as shown in Figure 10a,c. However, the big end of the connecting rod was not fully filled, which can be seen in Figure 10b. This was mainly because of the poor fluidity of the solid material during the SFF process resulting from the low sustaining temperature. Moreover, the big end of the connecting rod required a higher fluidity for the forming material in the SSF or SSFF processes compared with the rod shaft and the small end of the connecting rod. As shown in Figure 10d–f, the semi-solid connecting rod formed by the SSFF process with the RF of 75%, ST of 630 °C, and DT of 6 min exhibited a better shape profile compared to that from the SSF process. The smooth surface was obtained for the connecting rod from the SSFF process with no obvious crack, shrinkage, or any other defect. This indicated that the forming process for 7075 AACR is reasonable under the above process parameters, which in turn, verifies the feasibility and reliability of the SSFF process for AACRs in this work.

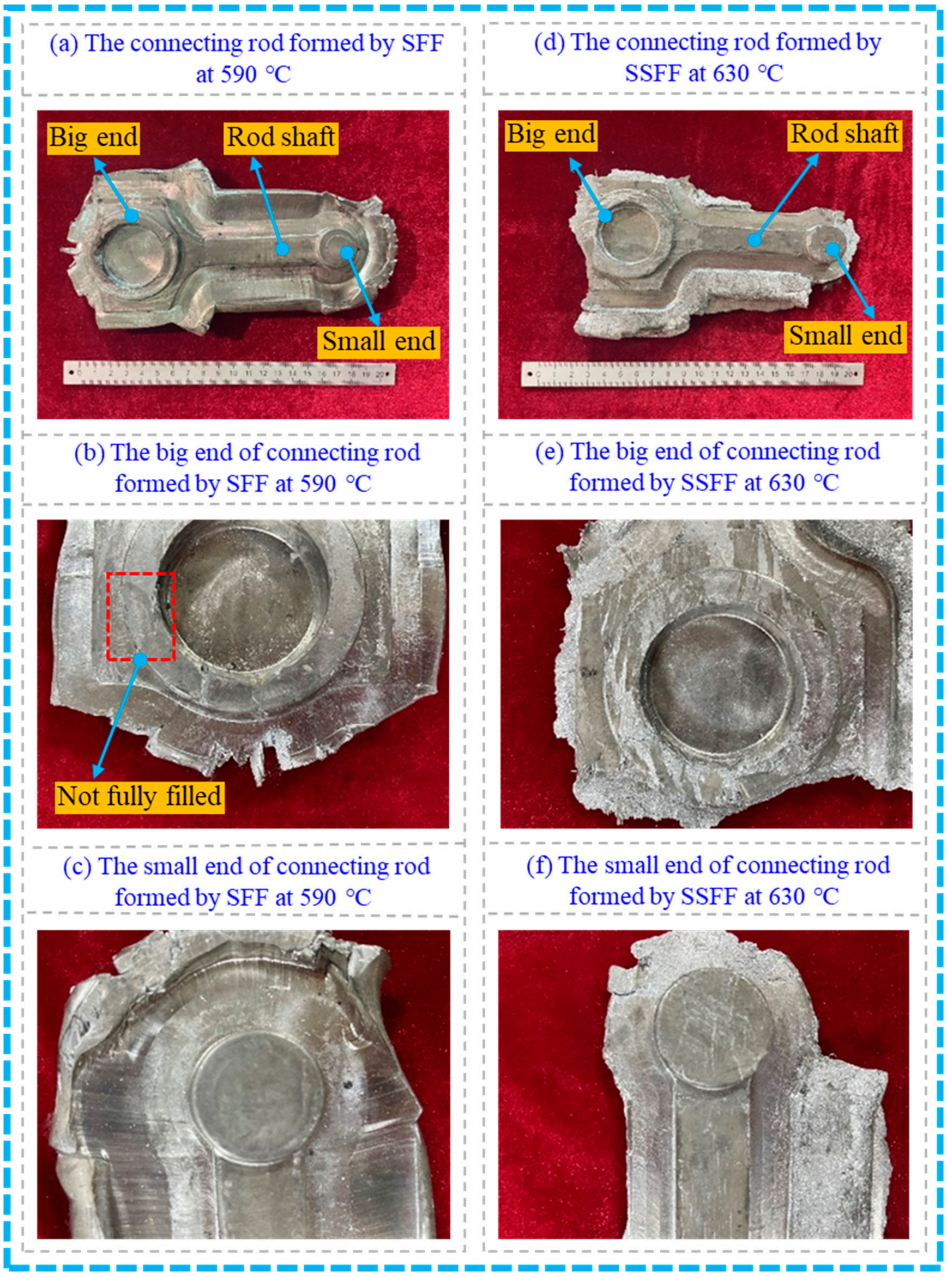

Figure 10. Macro-morphology of the connecting rod.

Microstructures at different positions of the connecting rod produced by the SFF and SSFF process are shown in Figure 11a,b, showing the longitudinal section microstructure of the sample in the rod shaft and the cross-section microstructure of the sample in the small end of the connecting rod formed by the SFF process, respectively. It was revealed that elongated shapes were observed in the grains in the longitudinal section microstructure at the center position of the connecting-rod shaft. However, uniform and fine grains were found in the cross-section microstructure at the position of the small end. It indicated that the grains of the connecting rod transformed into fibrous microstructures during the forging deformation in the SFF process. The longitudinal section microstructure of the rod shaft for the connecting rod formed by the SSFF process is provided in Figure 11c while that of the cross-section microstructure of the sample in the small end is shown in Figure 11d. It can be seen that the solid grain sizes in the longitudinal cross-section microstructure at the center position of the connecting-rod shaft and in the cross-section microstructure at the small end of the connecting rod were relatively uniform and spherical compared to that in Figure 11a,b. Moreover, no thick liquid film was observed between the solid grains. The AGS of the microstructure at the center of the connecting-rod shaft was obtained as 42.46 um, with a shape factor of 0.68. The AGS of the microstructure at the small end of the connecting rod was found to be 43.59 um, with a shape factor of 0.72. A comparison of the key indexes of the microstructures between the connecting rods prepared from SSB and SSFF in this work is provided in Table 4, which shows that the difference in grain size is not obvious, while the spheroidization degree of the solid grain was significantly reduced after the SSFF process. It indicated that the solid grain with the action of forging pressure produced localized plastic deformation during the SSFF process of connecting the rod. It also revealed that the deformation degree in the position of the connecting-rod shaft was larger than that in the position of the small end of the connecting rod.

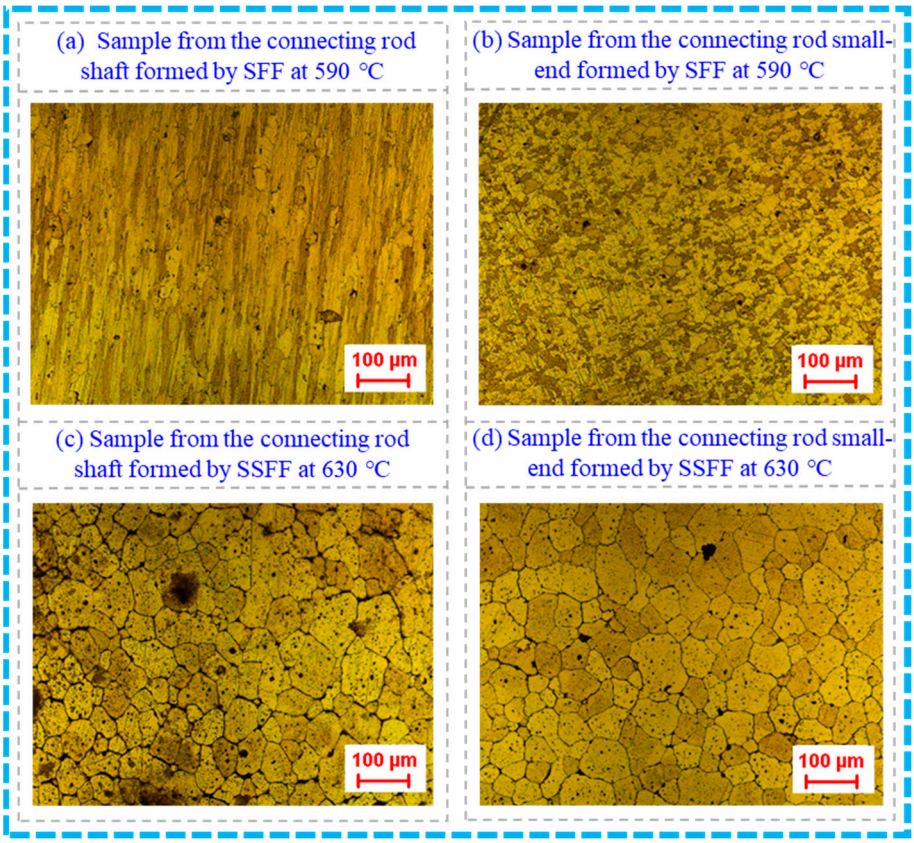

Figure 11. Microstructure of samples from different locations of the connecting rod.

Table 4. Microstructure analysis of the experimental result of the SSB and the connecting rod.

Experimental Result	AGS (μm)	SF
Semi-solid 7075 aluminum alloy billet	41.48~42.57	0.80~0.81
Connecting rod produced by SSFF process	42.46~43.59	0.68~0.72

The mechanical properties of the connecting rod produced by the SFF and SSFF process are summarized in Table 5, in which the operating parameters are different. In the SFF process, the process parameters were set as the FR of 75%, ST of 590 °C, and DT of 6 min. In the SSFF process, the process parameters were set as the FR of 75%, ST of 630 °C, and DT of 6 min. As shown in Table 5, the yield strength of the connecting rod produced by the SFF process was 229.95 MPa, while that from the SSFF process was 338.18 MPa. It means that the yield strength was improved by the SSFF process, with an improvement ratio of 47.07%. It was also found that the tensile strength of the connecting rod produced by the SFF process was obtained as 347.75 MPa, which was elevated to 420.40 MPa in the connecting rod produced by the SSFF process. Therefore, the tensile strength of the connecting rod was improved by the SSFF process, achieving an improvement ratio of 20.89%. The improvement of both the yield and tensile strengths can be attributed to the decreased dimension and spheroidized shape in the solid grain for the connecting rod produced by the SSFF process.

Table 5. Mechanical property of the connecting rod formed by SFF and SSFF process.

Mechanical Property	The Connecting Rod Formed by the SFF Process	The Connecting Rod Formed by the SSFF Process	Improvement Ratio
Yield strength (MPa)	229.95	338.18	47.07%
Tensile strength (MPa)	347.75	420.40	20.89%

4. Conclusions

This paper proposed the SSFF process for the production of the connecting rod for a HICE. It experimentally investigated the effect of the operating parameters on the quality of the produced connecting rod. The main conclusions are provided below.

(1) The 7075 aluminum alloy with a diameter of 90 mm used in this work can be successfully deformed by the RFPD process, with an FR of up to 75%. The FR of 75% is identified as a reasonable process parameter for the SSFF process proposed;
(2) In terms of the preparation of the 7075 aluminum alloy SSB, reasonable process parameters are obtained as two sets. One set is an FR of 75%, ST of 620 °C, and DT of 9 min. Another set is an FR of 75%, ST of 630 °C, and DT of 6 min. With reasonable working parameters, the 7075 aluminum alloy SSB can be prepared with the AGS of 41.48~42.57 μm and the ASF of 0.80~0.81;
(3) When the connecting rod is produced with an FR of 75%, ST of 590 °C, and DT of 6 min in the SFF process, the big end of the connecting rod is not fully filled, although the rod shaft and the small end of the connecting rod can be fully formed;
(4) An improved shape profile is obtained for the AACR formed by the SSFF process compared to that from the SFF process. The improvement ratios of yield strength and tensile strength by the SSFF process are 47.07% and 20.89%, respectively.

Author Contributions: Conceptualization, Y.W.; methodology, Y.W. and H.J.; validation, Y.W., C.Z. and H.J.; formal analysis, H.J., C.Z. and D.D.; investigation, Y.W., Y.G. and S.Z.; writing—original draft preparation, M.Z. and Y.W.; writing—review and editing, Y.G. and S.Z.; visualization, M.Z. and D.D. All authors have read and agreed to the published version of the manuscript.

Funding: This work is supported by the National Natural Science Foundation of China (Grant No. 52105397) and the Open Foundation of the National Key Laboratory of Metal Forming Technology and Heavy Equipment (Grant No. S2208100.W01).

Institutional Review Board Statement: Not applicable.

Informed Consent Statement: Not applicable.

Data Availability Statement: The data presented in this study are available upon request from the corresponding author. The data are not publicly available, due to the project's confidentiality requirements.

Conflicts of Interest: The authors declare no conflicts of interest.

Abbreviations

Abbreviations	Full Names
A	the area of the solid grain (μm^2)
AGD	average grain dimension of the solid grains (μm)
ASF	average shape factor of solid grains
N	number of solid grains
P	perimeter of the solid grain (μm)
HICE	hydrogen internal combustion engine
SSFM	semi-solid forming of metal
IHT	isothermal heat treatment
SIMA	strain-induced melt activation
ECAP	equal-channel angular pressing
RUE	repetitive upsetting extrusion
AACR	aluminum alloy connecting rod
DT	duration time (min)
FR	forging ratio
RFPD	radial forging plastic deformation
RF	radial forging
ST	sustaining temperature (°C)
IHT	isothermal heat treatment
SSB	semi-solid blank
RAP	recrystallization and partial remelting
SFF	solid forging forming
SSIT	semi-solid isothermal treatment
RFSIMA	Strain-induced melt activation

References

1. Hassan, Q.; Algburi, S.; Sameen, A.Z.; Salman, H.M.; Jaszczur, M. Green hydrogen: A pathway to a sustainable energy future. *Int. J. Hydrog. Energy* **2024**, *50*, 310–333. [CrossRef]
2. Gordon, J.A.; Balta-Ozkan, N.; Nabavi, S.A. Hopes and fears for a sustainable energy future: Enter the hydrogen acceptance matrix. *Int. J. Hydrog. Energy* **2024**, *60*, 1170–1191. [CrossRef]
3. Wang, Y.; Xiong, L.; Feng, D.; Liu, X.; Zhao, S. Research Progress on the Manufacturing of Screw-Shaped Parts in Screw Compressors. *Appl. Sci.* **2024**, *14*, 1945. [CrossRef]
4. Zhou, H.; Dai, J.; Chen, X.; Hu, B.; Wei, H.; Cai, H.H. Understanding innovation of new energy industry: Observing development trend and evolution of hydrogen fuel cell based on patent mining. *Int. J. Hydrog. Energy* **2024**, *52*, 548–560. [CrossRef]
5. Boretti, A. A high-efficiency internal combustion engine using oxygen and hydrogen. *Int. J. Hydrog. Energy* **2024**, *50*, 847–856. [CrossRef]
6. Güler, İ.; Kılıçaslan, A.; Küçük, T.; Corsini, D. Transient and altitude performance analysis of hydrogen fuelled internal combustion engines with different charging concepts. *Int. J. Hydrog. Energy* **2024**, *49*, 1112–1122. [CrossRef]
7. Azeem, N.; Beatrice, C.; Vassallo, A.; Pesce, F.; Gessaroli, D.; Biet, C.; Guido, C. Experimental study of cycle-by-cycle variations in a spark ignition internal combustion engine fueled with hydrogen. *Int. J. Hydrog. Energy* **2024**, *60*, 1224–1238. [CrossRef]
8. El-Adawy, M.; Nemitallah, M.A.; Abdelhafez, A. Towards sustainable hydrogen and ammonia internal combustion engines: Challenges and opportunities. *Fuel* **2024**, *364*, 131090. [CrossRef]
9. Qin, Z.; Liu, F.; Zhang, H.; Wang, X.; Yin, C.; Weng, W.; Han, Z. Study of hydrogen injection strategy on fuel mixing characteristics of a free-piston engine. *Case Stud. Therm. Eng.* **2024**, *56*, 104279. [CrossRef]
10. Yao, Z.; Li, W. Microstructure and thermal analysis of APS nano PYSZ coated aluminum alloy piston. *J. Alloys Compd.* **2020**, *812*, 152162. [CrossRef]
11. Li, X.; Guo, Y.; Xiong, W.; Jia, X.; Peng, X. Fracture mechanism and fault evolution of piston rod in hydrogen reciprocating compressor. *Int. J. Hydrog. Energy* **2024**, *50*, 942–958. [CrossRef]

12. Algayyim, S.J.M.; Saleh, K.; Wandel, A.P.; Fattah, I.M.R.; Yusaf, T.; Alrazen, H.A. Influence of natural gas and hydrogen properties on internal combustion engine performance, combustion, and emissions: A review. *Fuel* **2024**, *362*, 130844. [CrossRef]
13. Di Angelo, L.; Mancini, E.; Di Stefano, P. Numerical methodology for design and optimization of a connecting rod for very high speed engines. *Int. J. Interact. Des. Manuf.* **2022**, *16*, 109–134. [CrossRef]
14. Sathish, T.; Kumar, S.D.; Karthick, S. Modelling and analysis of different connecting rod material through finite element route. *Mater. Today Proc.* **2020**, *21*, 971–975. [CrossRef]
15. Saheb, S.H. Design and analysis of connecting rod with different materials for high fatigue life. *AIP Conf. Proc.* **2020**, *2283*, 020027.
16. Samat, S.; Omar, M.; Mohamed, I. Microstructural evolution and mechanical properties of thixoformed Al-Si-Cu alloy connecting rods. *Mater. Today Proc.* **2022**, *66*, 2705–2709. [CrossRef]
17. Schöbel, M.; Fernández, R.; Koos, R.; Bernardi, J. Elasto-plastic deformation in Al-Cu cast alloys for engine components. *J. Alloys Compd.* **2019**, *775*, 617–627. [CrossRef]
18. Niu, P.; Fu, H.; Zhang, H.; Guo, Y.; Stelmakh, O. Study on Oil Supply Characteristics of Connecting Rod Small End Bearing with Splash Lubrication by Smooth Particle Hydrodynamics Method. *J. Tribol.* **2024**, *146*, 044102. [CrossRef]
19. Apfelbacher, L.; Davids, A.; Hitzler, L. Development of a Lightweight Connection Rod for Motorbikes Fabricated with Hybrid Manufacturing. In *Collaborative Research Advancing Engineering Solutions for Real-World Challenges: The 2023 Postgraduate Seminar in Esslingen*; Springer: Cham, Switzerland, 2024; pp. 57–68.
20. Jayant, J.; Sahu, J. Design and Development of Connecting Rod with Aluminum Alloy Replacing Iron Based Alloy Material for Reciprocating Piston Engine. *Int. J. Technol. Res. Manag. ISSN* **2015**, *2*, 2348–9006.
21. Hawryluk, M.; Dudkiewicz, Ł.; Polak, S.; Barełkowski, A.; Miżejewski, A.; Szymańska, T. Improvement of the Technology of Precision Forging of Connecting Rod-Type Forgings in a Multiple System, in the Aspect of the Possibilities of Process Robotization by Means of Numerical Modeling. *Materials* **2024**, *17*, 1087. [CrossRef]
22. Winiarski, G.; Dziubińska, A. Analysis of a New Process of Forging a 2017A Aluminum Alloy Connecting Rod. *J. Manuf. Sci. Eng.* **2021**, *143*, 081006. [CrossRef]
23. Dziubinska, A. The New Technology of Die Forging of Automotive Connecting Rods from EN AB-71100 Aluminium Alloy Cast Preforms. *Materials* **2023**, *16*, 2856. [CrossRef] [PubMed]
24. Gupta, P.; Trivedi, A.K.; Gupta, M.; Dixit, M. Metal matrix composites for sustainable products: A review on current development. *Proc. Inst. Mech. Eng. Part L J. Mater. Des. Appl.* **2024**. [CrossRef]
25. Sulamet-Ariobimo, R.; Santoso, J.; Fadhlan, M.; Yasin, T.; Sukarnoto, T.; Mujalis, Y.; Oktaviano, Y. The effects of austenitizing process to mechanical properties of thin wall ductile iron connecting rod. *AIP Conf. Proc.* **2020**, *2262*, 060006.
26. Wang, Y.; Zhao, S.; Zhang, C. Microstructures and mechanical properties of semi-solid squeeze casting ZL104 connecting rod. *T. Nonferr. Metal. Soc.* **2018**, *28*, 235–243. [CrossRef]
27. Jiang, Y.; Le, Q.; Zhu, Y.; Liao, Q.; Wang, T.; Bao, L.; Wang, P. Review on forming process of magnesium alloy characteristic forgings. *J. Alloys Compd.* **2024**, *970*, 172666. [CrossRef]
28. Spencer, D.B.; Mehrabian, R.; Flemings, M.C. Rheological behavior of Sn15 pct Pb in the crystallization range. *Metall. Mater. Trans. B* **1972**, *3*, 1925–1932. [CrossRef]
29. Chen, H.; Xiao, H.; Cui, Y.X.; Zhou, Y.H. Effect of Solution Treatment on the Microstructure and Properties of Thixotropic Back-Extruded Copper Alloy Bushings. *J. Mater. Eng. Perform.* **2023**, *32*, 773–781. [CrossRef]
30. Chen, G.; Zhang, S.; Zhang, H.; Han, F.; Wang, G.; Chen, Q.; Zhao, Z. Controlling liquid segregation of semi-solid AZ80 magnesium alloy by back pressure thixoextruding. *J. Mater. Process. Tech.* **2018**, *259*, 88–95. [CrossRef]
31. Salleh, M.S.; Omar, M.Z.; Alhawari, K.S.; Mohammed, M.N.; Ali, M.A.M.; Mohamad, E. Microstructural evolution and mechanical properties of thixoformed A319 alloys containing variable amounts of magnesium. *T. Nonferr. Metal. Soc.* **2016**, *26*, 2029–2042. [CrossRef]
32. Xie, L.; Li, Y.; Zhou, R.; Li, Z.; Wang, Q.; Zhang, L.; Ji, Q.; Xu, B. Effect of Pouring Temperature on Microstructure Characteristics and Properties of Semi-Solid Near-Eutectic Al–Si Alloy. *Met. Mater. Int.* **2024**, *30*, 1479–1491. [CrossRef]
33. Cao, M.; Zhang, Q.; Zhang, Y. Effects of plastic energy on thixotropic microstructure of C5191 alloys during SIMA process. *J. Alloys Compd.* **2017**, *721*, 220–228. [CrossRef]
34. Hu, Y.; Liu, Y. Constitutive behavior of semi-solid $Al_{80}Mg_5Li_5Zn_5Cu_5$ light-weight high entropy alloy. *J. Mater. Res. Technol.* **2024**, *29*, 5713–5720. [CrossRef]
35. Huang, M.; Jiang, J.; Wang, Y.; Liu, Y.; Zhang, Y.; Dong, J.; Cui, J. Unraveling solid–liquid phase transition and microstructural coarsening of semi-solid $Al_{0.8}Co_{0.5}Cr_{1.5}CuFeNi$ HEA with dual globules for thixoforming application. *Mater. Design* **2024**, *237*, 112605. [CrossRef]
36. Xu, Y.; Chen, C.; Jia, J.; Zhang, X.; Dai, H.; Yang, Y. Constitutive behavior of a SIMA processed magnesium alloy by employing repetitive upsetting-extrusion (RUE). *J. Alloys Compd.* **2018**, *748*, 694–705. [CrossRef]
37. Jiang, H.; Dong, P.; Zhang, P.; Wang, Y.; An, L.; Li, H.; Zhao, S. Metal flowing and microstructure characteristics of the micro inner gear ring fabricated by rheological extrusion. *Int. J. Adv. Manuf. Technol.* **2024**, *131*, 1587–1600. [CrossRef]
38. Ma, X.; Abd Razak, N.; Ahmad, A. Semisolid metal processing parameters and metallurgical properties: An overview. *AIP Conf. Proc.* **2024**, *2998*, 060004.

39. Jiang, H.; Dong, P.; Zhang, P.; Wang, Y.; Li, F.; Zhu, C.; Meng, D.-A.; Fan, S.; Zhao, S. Deformation behavior and microstructure characterization of the radially forged 2A50 aluminum alloy at high-temperature solid and semi-solid states. *J. Alloys Compd.* **2024**, *989*, 174392. [CrossRef]
40. Li, Z.; Li, Y.; Zhou, R.; Xie, L.; Wang, Q.; Zhang, L.; Ji, Q.; Xu, B. Microstructure and properties of semi-solid 7075 aluminum alloy processed with an enclosed cooling slope channel. *Crystals* **2023**, *13*, 1102. [CrossRef]
41. Gu, G.; Li, R.; Xiang, L.; Xiao, G.; Lu, Y. Effects of Heating Rates on Microstructural Evolution of Hot Extruded 7075 Aluminum Alloy in the Semi-Solid State and Thixotropic Deformation Behavior. *Materials* **2023**, *16*, 6145. [CrossRef]
42. Jiang, J.; Tong, Z.; Huang, M.; Wang, Y.; Zhao, W. Effect of recrystallization annealing on microstructure and properties of cold-deformed $CoCrCu_{1.2}FeNi$ high entropy alloy. *J. Alloys Compd.* **2024**, *973*, 172943. [CrossRef]
43. Chang, M.; Liu, B.; Wang, Y.; Li, S.; Zhao, S. Effect of cross-sectional reduction ratio on microstructure evolution of semi-solid 7075 aluminum alloy prepared by RFSIMA process. *J. Alloys Compd.* **2024**, *989*, 174355. [CrossRef]
44. Xiao, G.; Jiang, J.; Liu, Y.; Wang, Y.; Guo, B. Recrystallization and microstructure evolution of hot extruded 7075 aluminum alloy during semi-solid isothermal treatment. *Mater. Charact.* **2019**, *156*, 109874. [CrossRef]
45. Xiao, G.-F.; Jiang, J.-F.; Ying, W.; Liu, Y.-Z.; Zhang, Y.; Guo, B.-Y.; Zhen, H.; Xian, X.-R. Microstructure and mechanical properties of 7075 aluminum alloy parts formed by semi-solid thixoextrusion. *T. Nonferr. Metal. Soc.* **2023**, *33*, 3235–3249. [CrossRef]
46. Fu, J.L.; Jiang, H.J.; Wang, K.K. Influence of Processing Parameters on Microstructural Evolution and Tensile Properties for 7075 Al Alloy Prepared by an ECAPBased SIMA Process. *Acta. Metall. Sin.* **2018**, *31*, 337–350. [CrossRef]
47. Binesh, B.; Aghaie-Khafri, M. RUE-based semi-solid processing: Microstructure evolution and effective parameters. *Mater. Design* **2016**, *95*, 268–286. [CrossRef]
48. Liu, J.; Cheng, Y.-S.; Chan, S.W.N.; Sung, D. Microstructure and mechanical properties of 7075 aluminum alloy during complex thixoextrusion. *T. Nonferr. Metal. Soc.* **2020**, *30*, 3173–3182. [CrossRef]
49. Meshkabadi, R.; Faraji, G.; Javdani, A.; Fata, A.; Pouyafar, V. Microstructure and homogeneity of semi-solid 7075 aluminum tubes processed by parallel tubular channel angular pressing. *Met. Mater. Int.* **2017**, *23*, 1019–1028. [CrossRef]
50. Mohammadi, H.; Ketabchi, M.; Kalaki, A. Microstructure Evolution of Semi-Solid 7075 Aluminum Alloy During Reheating Process. *J. Mater. Eng. Perform.* **2011**, *20*, 1256–1263. [CrossRef]
51. Wang, Y.-F.; Guo, Y.; Zhao, S.-D.; Fan, X.-G. Direct preparation of semi-solid billets by the semi-solid isothermal heat treatment for commercial cold-rolled ZL104 aluminum alloy. *Int. J. Min. Met. Mater.* **2021**, *28*, 1164–1173. [CrossRef]
52. Wang, Y.; Zhao, S.; Guo, Y.; Liu, K.; Zheng, S. Deformation Characteristics and Constitutive Equations for the Semi-Solid Isothermal Compression of Cold Radial Forged 6063 Aluminium Alloy. *Materials* **2021**, *14*, 194. [CrossRef] [PubMed]
53. Zou, J.; Ma, L.; Zhu, Y.; Jia, W.; Han, T.; Yuan, Y.; Qin, G. Deformation mechanism of ZK60 magnesium bars during radial forging: Mathematical modeling and experimental investigation. *Mater. Charact.* **2021**, *179*, 111321. [CrossRef]
54. Hu, X.; Han, X.; Chai, F.; Zhuang, W.; Zheng, F.; Yin, F.; Xie, L.; Hua, L. Efficiently manufacturing large-scale isotropic Al7075 alloy sheets with submicron grain by multidirectional rotary forging. *Mater. Design* **2024**, *238*, 112713. [CrossRef]
55. Zou, J.; Ma, L.; Jia, W.; Le, Q.; Qin, G.; Yuan, Y. Microstructural and mechanical response of ZK60 magnesium alloy subjected to radial forging. *J. Mater. Sci. Technol.* **2021**, *83*, 228–238. [CrossRef]
56. Zou, J.; Ma, L.; Zhu, Y.; Qin, L.; Yuan, Y. Gradient microstructure and superior strength–ductility synergy of AZ61 magnesium alloy bars processed by radial forging with different deformation temperatures. *J. Mater. Sci. Technol.* **2024**, *170*, 65–77. [CrossRef]
57. Gautam, S.K.; Singh, B.K. Investigation on the effects of isothermal holding temperature and time on the coarsening mechanism and rheological properties of ADC12 Al semi-solid slurry. *Mater. Chem. Phys.* **2024**, *314*, 128813. [CrossRef]

Disclaimer/Publisher's Note: The statements, opinions and data contained in all publications are solely those of the individual author(s) and contributor(s) and not of MDPI and/or the editor(s). MDPI and/or the editor(s) disclaim responsibility for any injury to people or property resulting from any ideas, methods, instructions or products referred to in the content.